communications physics

A Nature Portfolio journal

Article

https://doi.org/10.1038/s42005-025-02066-5

Non-thermal electrons open the non-equilibrium pathway of the phase transition in FeRh

Maximilian Mattern [1,2], Steffen Peer Zeuschner[1], Matthias Rössle [3], Jon Ander Arregi [4], Vojtěch Uhlíř [4,5] & Matias Bargheer [1,3]

The optical excitation of metals initially creates short-lived non-Fermi distributions of the electrons. The electrons and holes excited far above and below the Fermi level quickly relax to hot Fermi-distributions that subsequently cool via electron-phonon scattering. Here, we show that such non-thermal charge carriers beyond the Fermi-distribution speed up the prototypical first-order antiferromagnetic-to-ferromagnetic phase transition in FeRh. In ultrafast x-ray diffraction experiments, we vary the maximum electron temperature by increasing the pump pulse duration up to 10 ps. For direct optical excitation of FeRh, ferromagnetic domains nucleate within 8 ps as soon as the successively deposited energy surpasses the site-specific threshold energy. In contrast, suppressing the direct optical excitation by an optically opaque Pt layer leads to a nucleation on a 50 ps timescale driven by the near-equilibrium heat transport. These findings unambiguously identify the photo-excitation of non-thermal electrons and not electron-phonon non-equilibria to enable the rapid phase transition in FeRh.

The selective excitation of electrons or phonons by femtosecond laser pulses drives solids into non-thermal states[1–7] and phases[8–11] and opens transition routes and kinetics[12–16] that are not accessible upon equilibrium heating. This includes coherent dynamics[7], non-equilibria among different subsystems[1,2] and non-thermal populations of certain degrees of freedom[1,2,5]. In addition to these non-thermal energy distributions, the laser-pulse can directly modify the electronic and magnetic structure via field-driven effects[17–19].

In materials featuring first-order phase transitions, a fine interplay of spin, charge, and lattice degrees of freedom[9,10,20–22] leads to an abrupt change of structural, electronic, and magnetic properties. In this context, the non-equilibria introduced by femtosecond laser-excitation may open novel non-thermal routes of the phase transition through transient phases with different properties[8,10,11,14] where individually tracking the different degrees of freedom can provide unique insights into the microscopic processes and driving mechanisms of the phase transition[8,9,20,22].

Since its discovery, the prototypical first-order magneto-structural antiferromagnetic-to-ferromagnetic (AFM-FM) phase transition of FeRh at 370 K was extensively studied due to its potential for future applications[23–26]. Previous studies proposed a variety of different mechanisms driving the phase transition, for example expansion-induced sign change of the exchange constant[27], excitation of spin waves[28] and dominant FM exchange of the Fe moments mediated by an induced Rh moment[21,29–33]. The latter was described as a competition between bilinear and higher order four spin exchange terms in atomistic spin dynamics[32], a combination of Heisenberg exchange of Fe and a Stoner model for Rh[30] and a modification of the Rh-Fe hybridization[21,31,33]. However, the microscopic pathway of the transition upon femtosecond laser-excitation is still under debate.

Previous time-resolved experiments individually tracked the evolution of the electronic, magnetic, and lattice degrees of freedom upon femtosecond laser excitation. While photoemission spectroscopy identified a rapid modification of the electronic band structure within the first picosecond[33], the formation of a macroscopic magnetization takes hundreds of picoseconds[34–36]. This is because a macroscopic magnetization requires the alignment of the nucleated FM domains whose magnetization initially points along different directions[35,36]. Thus, probing the macroscopic magnetization cannot measure the nucleation timescale of the FM domains. An established workaround is probing the lattice expansion that accompanies the phase transition via ultrafast x-ray diffraction (UXRD)[35,37–39]. The first UXRD experiments probed thick inhomogeneously photo-excited films and reported different rise times between 15 and 90 ps[35,37] for different excitation strength and probing depth. Recently, we related these

[1]Institut für Physik und Astronomie, Universität Potsdam, Potsdam, Germany. [2]Max-Born-Institut für Nichtlineare Optik und Kurzzeitspektroskopie, Berlin, Germany. [3]Helmholtz-Zentrum Berlin für Materialien und Energie GmbH, BESSY II, Berlin, Germany. [4]CEITEC BUT, Brno University of Technology, Brno, Czech Republic. [5]Institute of Physical Engineering, Brno University of Technology, Brno, Czech Republic. e-mail: bargheer@uni-potsdam.de

observations to two pathways of the phase transition with considerably different nucleation timescales[38]. In the near-surface region of thick FeRh films which is excited by femtosecond laser pulses, the FM phase nucleates on an 8 ps timescale while it takes 50 ps to transform the lower lying regions that are only excited via near-equilibrium heat transport. In case of a homogeneous optical excitation realized in laterally nano-structured FeRh films that favors plasmonic absorption, we exclusively observed the 8 ps timescale[39]. This illustrates that femtosecond laser-excitation unlocks the fast non-equilibrium pathway of the phase transition in FeRh.

However, it has remained unclear, which aspect of the femtosecond laser excitation is decisive for the pathway of the phase transition: is it necessary to have transient non-thermal electron distributions induced by a direct electron-photon interaction in FeRh? Or is it sufficient to have a strongly heated Fermi distribution that only influences the population of electronic states approximately 0.1 eV around the Fermi energy?

Here, we disentangle the role of electron–photon interactions and strongly elevated electron temperatures for the laser-induced phase transition in FeRh by utilizing pump pulses with picosecond duration combined with femtosecond x-ray probe pulses accessing the evolution of the structural order parameter. Irrespective of the pump pulse duration between 0.06 and 10.5 ps, we observe the FM phase to rise on an 8 ps timescale where the final FM volume fraction is exclusively given by the total deposited energy and the transition starts as soon as the successively deposited energy overcomes the site-specific threshold of the first-order phase transition. These results indicate the decisive role of photo-excited non-thermal charge carriers for the dynamics of the laser-induced first-order phase transition in FeRh. To cross-check this conclusion, we additionally performed experiments on a thin FeRh layer that is only indirectly excited by heat transport via thermalized electrons generated in an optically opaque Pt capping layer that suppresses the direct optical excitation of FeRh. Under this condition, the FM phase rises only on a 50 ps timescale irrespective of the excitation strength.

UXRD experiments

Figure 1a, c sketchs the sample structures consisting of epitaxial $L_{\mathrm{FeRh}} = 12$ nm thick FeRh(001) films grown by magnetron sputtering from an equiatomic FeRh target[40] on double-side polished MgO(001) substrates. The second sample is capped by a 31.6 nm thick Pt(001) layer, which is much thicker than the inelastic mean free path of the electrons (4 nm)[41] and the optical penetration depth ($\delta_{\mathrm{Pt}} = 9$ nm)[42]. Previous experiments with variable Pt capping layer thickness additionally reported a reduced heating of buried layers for thicknesses above 7 nm[42]. Therefore, the Pt capping layer ensures the indirect excitation of the buried FeRh layer by thermalized electrons. Figure 1b, d displays the temperature-dependent out-of-plane lattice constant d (symbols) and the magnetization M_{FeRh} (solid lines) of both samples. We find good agreement between the two order parameters of the phase transition. However, the hysteresis for this locally probed lattice constant is narrower than the global temperature-dependent magnetization due to the spatial heterogeneity of the transition temperature. The different average transition temperatures of the two samples originate from a lattice deformation induced by the Pt capping layer (see Methods section). The magnetization data indicate the presence of a residual FM phase of ≈20 % originating from interface effects[43–45]. This residual room-temperature FM phase is consistent with the reduced out-of-plane expansion across the phase transition of $\eta^{\mathrm{thin}}_{\mathrm{AFM-FM}} = 0.48\,\%$ compared to $\eta^{\mathrm{thick}}_{\mathrm{AFM-FM}} = 0.6\,\%$ observed in thicker films[38,39].

Figure 1a, c sketch the performed UXRD experiments including the depth profile of the optically deposited energy calculated in a transfer matrix formalism (see Methods section). The sample structures are excited by p-polarized pump pulses with a central wavelength of 800 nm. We probe the transient out-of-plane strain response of the FeRh layer via symmetric $\theta - 2\theta$ scans[46] with 200 fs hard x-ray pulses provided by a table-top laser-driven plasma x-ray source[47] (see Methods section for further details). The Bragg peak position along the reciprocal space coordinate q_z encodes the mean out-of-plane lattice constant d of the FeRh films via $q_z = 4\pi/d$. The lattice strain $\eta_{\mathrm{FeRh}} = \Delta d/d_0$ is the relative change Δd of the lattice constant with respect to its value d_0 before excitation. The bare FeRh film is excited by pump pulses of different durations between 0.06 and 10.5 ps realized by detuning a grating compressor.

Results and discussion

Phase transition driven by picosecond pump pulses

Figure 2a displays the laser-induced transient strain response of the bare FeRh film on MgO for a below-threshold excitation $F_{\mathrm{bt}} = 0.4$ mJ cm^{-2} with pump pulses of 60 fs and 5.2 ps duration that do not drive the AFM-FM phase transition. Thus, the strain response upon femtosecond laser excitation is the superposition of only two contributions: (i) A quasi-static expansion originating from heating the electrons and phonons of FeRh and (ii) propagating strain pulses driven by the rapidly rising unbalanced stress at the surface and the substrate interface upon femtosecond laser

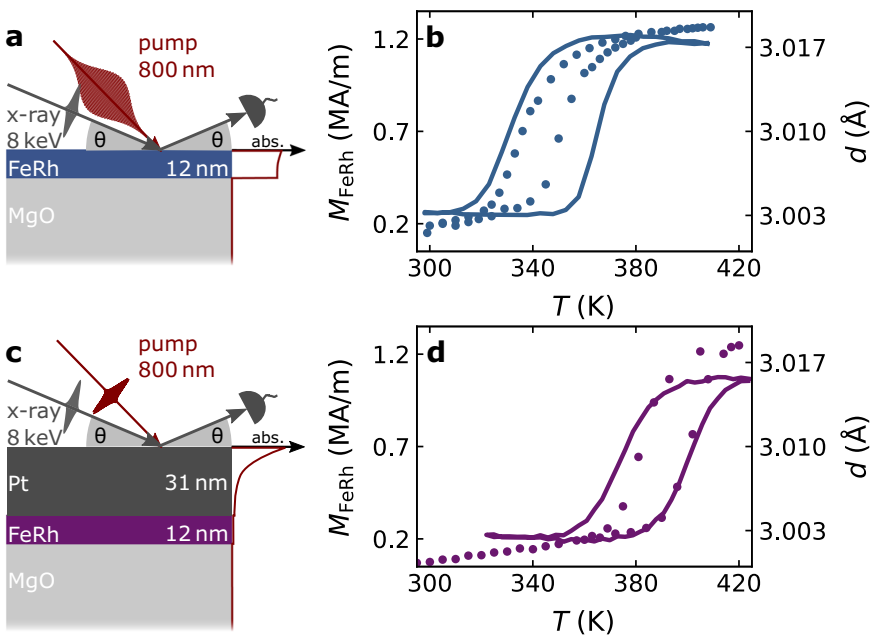

Fig. 1 | Static characterization of the FeRh films. **a** Sketch of the FeRh sample, the optical absorption profile and the ultrafast x-ray diffraction (UXRD) experiment, mapping the reciprocal space via $\theta - 2\theta$ scans. **b** Characterization of the antiferromagnetic-to-ferromagnetic phase transition in the bare FeRh film by the temperature-dependent magnetization (solid line) and the average out-of-plane lattice constant d (symbols). **c**, **d** Same as **a**, **b** for the sample with Pt capping layer.

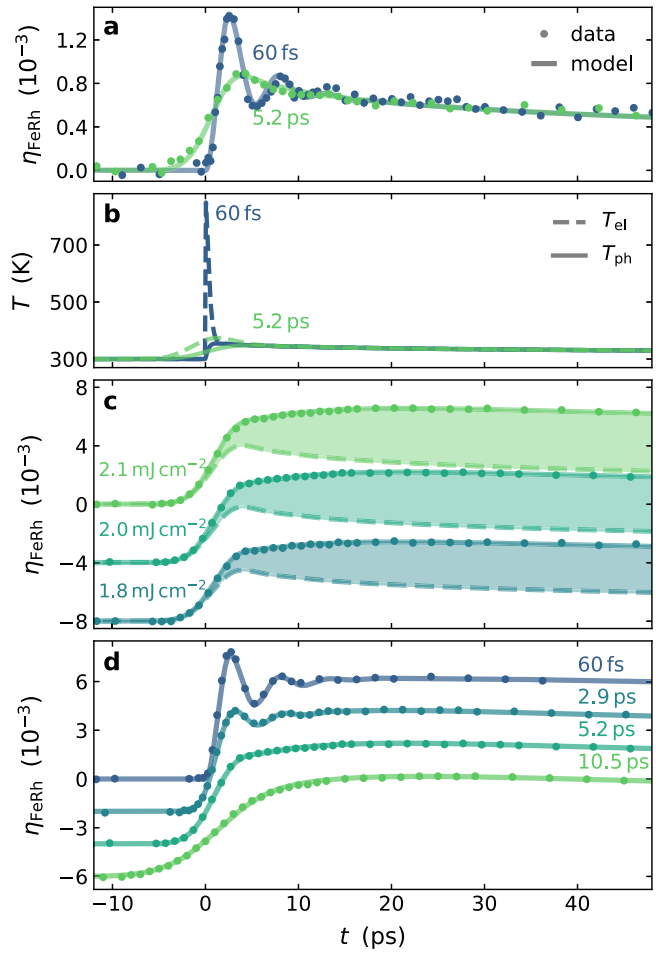

Fig. 2 | Transient strain response containing expansion from the phase transition. a Thermoelastic strain response to a below-threshold fluence of $F_{bt} = 0.4$ mJ cm^{-2} for 60 fs and 5.2 ps-long pump pulses (symbols). The solid lines denote the strain response modeled by utilizing the UDKM1DSIM library[49] and literature values for the thermo-elastic parameters. **b** The transient average electron (dashed lines) and phonon (solid lines) temperatures in FeRh extracted from the strain modeling by applying a diffusive two-temperature model (2TM). **c** The strain response to various above-threshold excitations with 5.2 ps-long pump pulses additionally includes signatures of the driven antiferromagnetic-to-ferromagnetic phase transition highlighted by the colored area representing the difference $\Delta\eta(t)$ between the measured strain (symbols) and the fluence-scaled thermoelastic strain (dashed lines). **d** The strain response for a fixed above-threshold fluence of $F_{at} = 2.1$ mJ cm^{-2} and various pump pulse durations (symbols). The solid lines in (**c**) and (**d**) are the sum of strain due to the phase transition according to Eq. (1) and the fluence-scaled sub-threshold strain response depicted in panel (**a**). The results are off-set for clarity.

excitation[48]. The launched strain pulse propagates with sound velocity v_s and is reflected at the surface and partially transmitted into the substrate. This leads to a decaying oscillation[48] with a period of $2L_{FeRh}/v_s$ that is superimposed with a decreasing quasi-static expansion due to heat transport into the substrate. The 5.2 ps pump pulse slowly heats FeRh. This drives a stress on the lattice which rises slower than its relaxation by lattice expansion with sound velocity. Therefore, pump pulses with durations significantly exceeding $2L_{FeRh}/v_s$ disable the coherent excitation of picosecond strain pulses and thus we only observe the slowly rising quasi-static expansion of FeRh. Since the strain pulse launched by femtosecond laser excitation completely enters the MgO substrate within 20 ps, the strain response for $t > 20$ ps is independent of the pump pulse duration.

The solid lines in Fig. 2a denote our strain model utilizing the modular PYTHON library UDKM1DSIM[49] and literature values for the thermoelastic parameters (see Methods section). We apply a diffusive two-temperature model (2TM) to describe the spatio-temporal distribution of the optically deposited energy among electrons and phonons. Their excitation drives the lattice response according to the linear one-dimensional elastic wave equation. We find excellent agreement of our model with the experiment, if we assume a Gaussian shape of the pump pulses and consider their experimentally determined durations. We emphasize that the green line, which represents the modeling for a 5.2 ps pump pulse is indistinguishable from the convolution of the strain model for 60 fs (blue line) with a Gaussian of 5.2 ps full-width half-maximum in case of a below-threshold excitation. This is consistent with the strictly linear thermoelastic strain response expected for metals as a function of the fluence[48]. Figure 2b displays the respective transient electron and phonon temperatures. While the electrons and phonons experience a pronounced non-equilibrium upon femtosecond laser-excitation, the 5.2 ps-long pump pulse suppresses this non-equilibrium by drastically reducing the maximum electron temperature because a considerable amount of energy is already dissipated to the phonons during the optical absorption.

In the following, we utilize this calibration of the thermoelastic strain η^{bt}_{FeRh} to extract the signatures of the AFM-FM phase transition from the strain response η^{at}_{FeRh} to above-threshold excitations in Fig. 2c, d. Figure 2c exemplarily displays the signature of the laser-induced phase transition to the strain response for various above-threshold excitations by pump pulses of 5.2 ps duration. The dashed lines denote the modeled thermoelastic strain contributions for $F_{bt} = 0.4$ mJ cm^{-2} (green solid line in a) scaled to the fluences F_{at} in the experiment. The difference to the actual measurement $\Delta\eta(t)$ highlighted by colored areas is related to an additional expansion that parametrizes the phase transition[38]. To determine the absolute value of the transient FM volume fraction, we consider the expansion across the phase transition in thermal equilibrium η^{thick}_{AFM-FM} and the latent heat Q_{AFM-FM} of the first-order phase transition. The latent heat is given by the integral of the contribution of the first-order phase transition to the heat capacity per volume $C_{AFM-FM}(T)$[50]. This energy required for transforming FeRh into the FM phase reduces the local temperature[51] by $\Delta T = Q_{AFM-FM}/C_{ph}$, which reduces the quasi-static expansion of FeRh by $\eta_{AFM} = \alpha_{AFM}\Delta T$ with the expansion coefficient α_{AFM} in the AFM phase. This relates $\Delta\eta(t) = \eta^{at}_{FeRh} - F_{at}/F_{bt} \cdot \eta^{bt}_{FeRh}$ to the laser-induced FM volume fraction ΔV_{FM} via:

$$\Delta\eta(t) = (\eta^{thick}_{AFM-FM} - \eta_{AFM})\Delta V_{FM}(t), \quad (1)$$

where the total FM fraction $V_{FM}(t) = \Delta V_{FM}(t) + V^0_{FM}$ additionally includes the residual FM phase $V^0_{FM} = 0.2$ present before the laser excitation as characterized in Fig. 1b. Figure 2d displays the strain response for systematically varied pump pulse durations and an excitation of 2.1 mJ cm^{-2} driving the phase transition as identified by the fluence dependence in Fig. 2c. With increasing pump pulse duration the oscillations in the strain response originating from coherently driven picosecond strain pulses are successively suppressed and completely vanish for 5.2 ps-long pump pulses. In contrast to the coherent dynamics, the expansion of FeRh beyond 20 ps is identical for all pump pulse durations. This already indicates that the final FM volume fraction V^*_{FM} is independent of the pump pulse duration.

Figure 3 displays the extracted laser-induced FM volume fraction $\Delta V_{FM}(t)$ that parameterizes the optically driven phase transition. For 60 fs pump pulses, $\Delta V_{FM}(t)$ in Fig. 3a is very well reproduced by a single exponential rise associated with the nucleation of domains[35] on an $\tau = 8$ ps timescale[38] by:

$$\Delta V_{FM}(t) = \mathcal{H}(t)\Delta V^*_{FM} \cdot \left(1 - e^{-t/\tau}\right), \quad (2)$$

with the Heaviside function $\mathcal{H}(t)$ and the final FM volume fraction increase ΔV^*_{FM} that depends on the fluence. For femtosecond laser excitation we previously calibrated[38] $\Delta V^*_{FM} > 0$ if $F > F_{th} = 0.6$ mJ cm^{-2}, $\Delta V^*_{FM} = 0.6$ for 1.8 mJ cm^{-2} and $\Delta V^*_{FM} = 0.8$ if $F = 2.1$ mJ cm^{-2}. This fluence dependence upon femtosecond laser excitation is perfectly reproduced by the

fluence-dependent $\Delta V_{FM}(t)$ upon excitation by 5.2 ps pump pulses in Fig. 3. This agreement demonstrates that the threshold of the first-order phase transition is insensitive to the duration of the pump pulse.

The dashed lines in Fig. 3 represent $\Delta V_{FM}(t)$ from Eq. (2) convoluted with a Gaussian representing the pump-pulse duration in the experiment. This approach assuming a linear response to the optical excitation was used to fit the laser-induced demagnetization in Ni associated with a second order phase transition[52]. However, for the first-order phase transition in FeRh this approach clearly deviates from the measurement for long pump pulses. With increasing pump pulse duration this deviation within the first picoseconds becomes more pronounced (see Fig. 3a). Interestingly, the data rise faster than the convolution although the rise starts later, which we attribute to the non-linearity associated with the threshold for the phase transition. This means that driving the phase transition also leads to a deviation between the strain response in Fig. 2c, d and a simple convolution of the strain response upon femtosecond excitation with a Gaussian. Thus, the effect of the ps-pump pulse on the strain response goes beyond a simple reduction of the time-resolution.

As an improved model of $\Delta V_{FM}(t)$ for long pump-pulses, we explicitly consider the successively deposited energy that leads to the unlocking of the AFM-FM phase transition in an increasing volume fraction of the film during the pump-pulse. This explicit treatment of the threshold character of first-order phase transitions extends Eq. (2) in the case of picosecond pump-pulses to

$$\Delta V_{FM}(t) = \int \mathcal{H}(t-t')V^*_{FM}(t') \cdot \left(1 - e^{-(t-t')/\tau}\right) dt'. \qquad (3)$$

Here, the FM volume fraction $V^*_{FM}(t')$ is unlocked at delay t' by the increase of the deposited energy and subsequently rises on the $\tau = 8$ ps nucleation timescale. This transiently unlocked phase transition adds to the already present FM phase driven at delays $t < t'$. The Heaviside function $\mathcal{H}(t-t')$ ensures a start of the phase transition at t'. To model the transient FM volume fraction we assume a linear increase of V^*_{FM} from 0 to 0.8 between the fluences $F_{th} = 0.6$ mJ cm^{-2} and 2.1 mJ cm^{-2}, which corresponds to a full phase transition[38].

Under this assumption, Eq. (3) yields excellent agreement (solid lines) with the experimentally determined transients $\Delta V_{FM}(t)$ in Fig. 3a, b for various pump-pulse durations and above-threshold fluences. The model also agrees very well with the measured dependence of the transient strain on the fluence and pulse duration in Fig. 2c, d. The solid lines represent the sum $\eta^{at}_{FeRh}(t) = F_{at}/F_{bt} \cdot \eta^{bt}_{FeRh}(t) + \Delta\eta(t)$, i.e., the fluence-scaled thermoelastic below threshold strain plus the strain contribution $\Delta\eta(t)$ determined in Fig. 3 using Eqs. (3) and (1). Our model accounts for the threshold of the first-order phase transition. Therefore it can reproduce both the delayed start of the nucleation of FM domains relative to the beginning of the pump pulse for longer pump-pulses and decreasing fluence. Furthermore, it demonstrates that the nucleation of FM domains proceeds on the intrinsic 8 ps timescale upon laser excitation even for 10.5 ps long pump pulses that suppress any electron–phonon non-equilibrium.

Phase transition driven by near-equilibrium heating

These results obtained in a homogeneously excited 12 nm FeRh film show that the direct optical excitation always triggers the phase transition within 8 ps. On the other hand, our recent experiment on thicker inhomogeneously excited FeRh films show that longer timescales may apply in the deeper parts of the film, which are not directly optically excited[38]. In order to cross-check this insight in a more directly comparable FeRh thin film, we performed an UXRD experiment using 60 fs pump pulses on a similar 12 nm thin FeRh film buried below an optically opaque Pt layer (see Fig. 1c) that suppresses the direct optical excitation of FeRh. It is then only excited by heat transport via thermalized electrons.

As for the sample without Pt cap, we measured and modeled the strain response of the FeRh layer to a below-threshold excitation. To make our modeling more reliable, we additionally measured and modeled the strain response of the Pt capping layer. Figure 4 shows an excellent agreement of our model with the transient strain response of both Pt and FeRh with a single set of parameters (see Methods section). Pronounced features of the dynamics are the direct expansion of Pt and the clear 8.5 ps delay of the sharp onset of the FeRh expansion, that precisely matches the time that the longitudinal acoustic strain pulse takes to travel through Pt. Figure 4b displays the associated average electron and phonon temperatures in FeRh. We find a relatively slow heating of the electrons within the first picosecond via heat diffusion from Pt. This indirect excitation leads to a delay of the FeRh expansion with respect to the Pt capping layer (see Fig. 4a). Figure 4b shows a rapidly rising average phonon temperature in FeRh within 3 ps due to the strong electron–phonon coupling. However, this fast heating of FeRh is spatially inhomogeneous since the strong electron–phonon coupling localizes the electronic heat input near the Pt interface (see Fig. 4c). This results in a slow equilibration of the phonon temperature within tens of picoseconds across the 12 nm FeRh film, which is only homogeneously heated after 30 ps.

With our model for the thermoelastic strain contribution at hand, we extract the additional expansion contribution associated with the driven AFM-FM phase transition $\Delta\eta(t)$ from the strain response to above threshold excitations $\eta_{at}(t)$ shown in Fig. 4d. The solid lines denote the thermoelastic strain contribution scaled to the fluence and the deviation to the actual measurement directly identifies the laser-induced phase transition. By applying Eq. (1), we extract the corresponding change of the FM volume fraction ΔV_{FM} (see Fig. 4e). The gray solid lines denote a fit of the transient FM volume fraction by a single exponential with a variable timescale and a

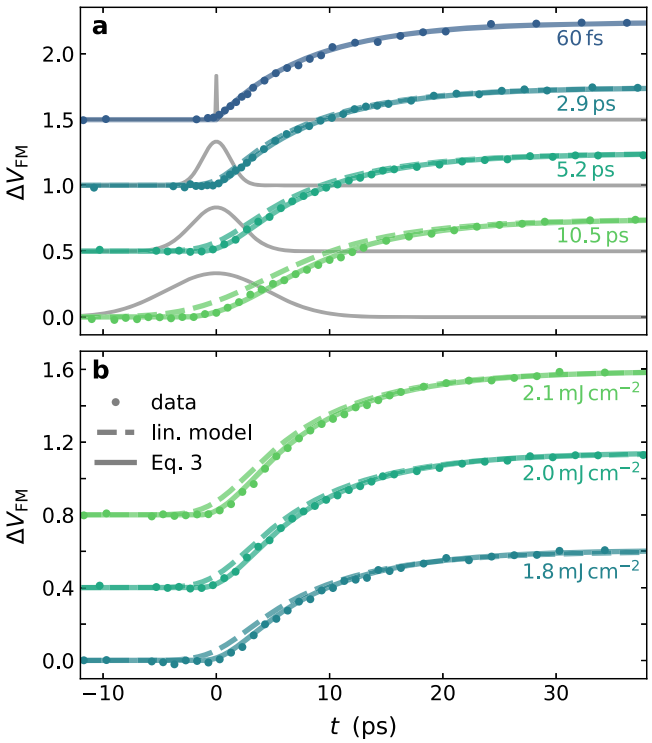

Fig. 3 | Phase transition induced by picosecond pump pulses. a Laser-induced rise of the ferromagnetic (FM) volume fraction ΔV_{FM} (symbols) for different pump-pulse durations (assumed pulse profile indicated by gray solid lines) and a fluence of $F_{at} = 2.1$ mJ cm^{-2}. **b** Laser-induced rise of ΔV_{FM} (symbols) for various above-threshold excitations and 5.2 ps pump-pulse duration. In both panels, the dashed lines represent the FM volume fraction according to Eq. (2), i.e., for ultrashort pulse excitation, convoluted with a Gaussian representing the duration of the respective pump-pulse. The data rise faster but start delayed compared to the dashed lines, which correspond to a linear response via the convolution. The solid lines show the appropriate model for the FM volume fraction according to Eq. (3), which accounts for the non-linear threshold behavior. The plots are off-set for clarity.

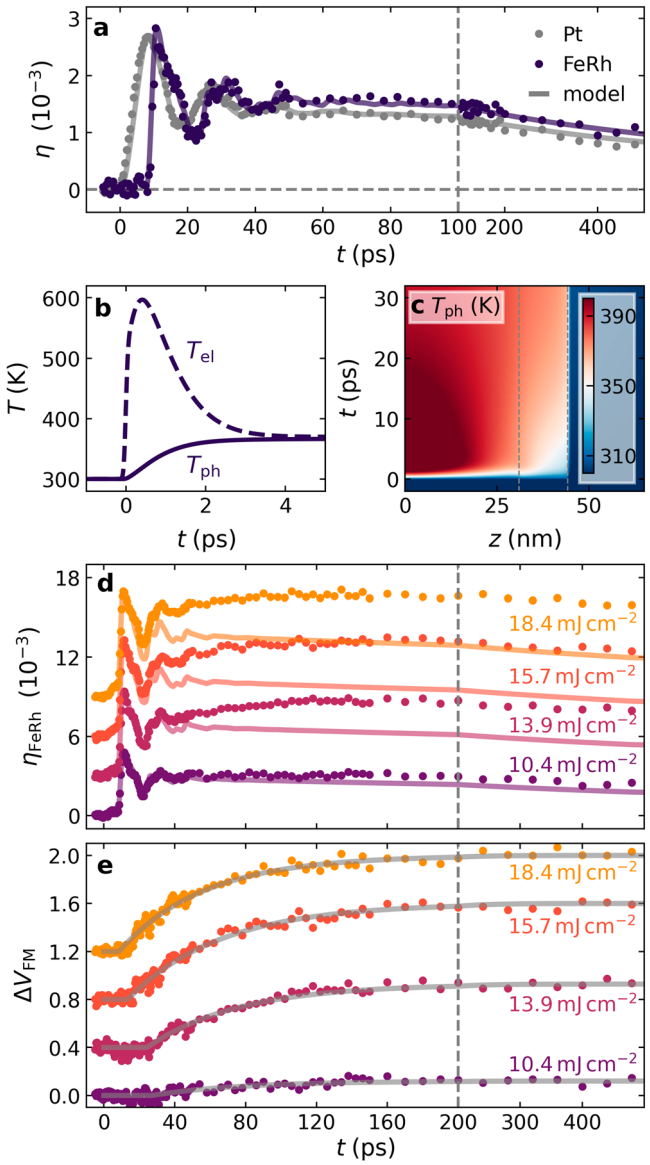

Fig. 4 | Dynamics of phase transition in case of suppressed direct optical excitation. a The strain response of the Pt and the FeRh layer (symbols) to a below-threshold fluence of F_{bt} = 5.8 mJ cm^{-2}. The solid lines represent the modeled strain (see Methods section). **b** The average electron (dashed line) and phonon (solid line) temperatures in FeRh extracted from the diffusive two-temperature model (2TM) of the strain modeling for the same fluence. **c** The corresponding spatio-temporal phonon temperature T_{ph} as function of the delay t and the distance to the surface z. The colorbar quantifies the initially inhomogeneous phonon temperature upon laser excitation. **d** The strain response of FeRh to above-threshold excitations (symbols). The additional expansion compared to the modeled thermoelastic strain response (solid lines) is a clear signature of the laser-induced phase transition. **e** Extracted transient change of the ferromagnetic (FM) volume fraction ΔV_{FM} according to Eq. (1) (symbols). The gray solid lines denote a single exponential fit with an average rise time of 50.7 ± 1.9 ps. The results in (**d**) and (**e**) are off-set for clarity.

variable offset time t_T at which the FM phase transition starts. Irrespective of the excitation strength, we find a τ_{eq} = 50.7 ± 1.9 ps timescale for the rise of the FM phase according to $1 - e^{-(t-t_T)/\tau_{eq}}$.

All data in Fig. 4d can be fitted with the same τ_{eq}, with the clear trend that higher fluences lead to an earlier start t_T of the nucleation and a larger converted volume fraction ΔV^*_{FM}. However, the precise timing and amplitude of the emerging FM phase is not described by our straightforward thermodynamic model that yields the excellent agreement with the sub-threshold strain in Fig. 4a. Although, the fluence scaling reproduces the acoustic strain waves in the first 40 ps in Fig. 4c, the modeled phonon temperature in FeRh for indirect excitation through Pt at 10.4 mJ cm^{-2} exceeds 440 K. According to the characterization in thermal equilibrium in Fig. 1d, this should drive a full phase transition in the entire film and not only in 15 %. Even if we consider the energy consumed by the latent heat of the phase transition and the enhanced transition temperature due to the laser-induced tetragonal distortion of the unit cell by 4 K per 0.1 % out-of-plane expansion[25], we would still expect a complete phase transition from the behavior in thermal equilibrium. Furthermore, the delay t_T at which the phase transition starts, is not simply given by the time at which the phonon temperature exceeds the equilibrium phase transition temperature. For higher fluences (15.7 and 18.4 mJ/cm^2) the nucleation starts at about 8.5 ps and for lower fluences at about 25 ps. The latter qualitatively agrees with the time it takes to heat the near-substrate region above the transition temperature (see Fig. 4c). This indicates that under near-equilibrium heating the FM phase emerges similar to experiments in thermal equilibrium that reported a nucleation of FM domains as columns through the entire film[53]. Assuming that the columnar grains composing our epitaxial film[40] act as a fundamental block for the phase transition, the top part of the FeRh film cannot transition until the bottom part is sufficiently heated, too. In a simple picture, this means that the FM phase can only emerge when the phonon temperature exceeds the transition temperature through the entire thickness of the FeRh film. Furthermore, we find a coincidence between the start of the nucleation and the time when the expansion wave launched at the Pt surface or its back reflection enters FeRh at 8.5 ps or 25 ps, respectively (Fig. 4d). This suggest that the nucleation of the FM phase in a superheated AFM state of FeRh is started by an impulsive expansion, similar to the nucleation of ice in a supercooled liquid[54]. Despite the fact that the coherent strain pulse must be faster than the diffusion of heat via phonons, the first strain wave can indeed impinge on a superheated FeRh as the electrons rapidly transport energy from Pt into FeRh according to the 2TM (Fig. 4c).

To cross-check that the observed 50 ps nucleation timescale upon near-equilibrium heating indeed originates from the excitation condition, we compare all-optical reflectivity measurements upon laser-excitation from the Pt-side (as in the UXRD experiment) to excitation through the MgO-substrate (direct photo-excitation of FeRh). For experimental details we refer to the Methods section. Figure 5 shows that for fluences exceeding the transition threshold an additional change in the reflectivity appears that originates from the lattice expansion induced by the phase transition. This additional contribution probes the emergence of the FM phase[30]. In our experiment it rises on a 50 ps timescale upon excitation from the Pt-side (Fig. 5a) but on an 8 ps timescale upon direct photo-excitation through the MgO substrate (Fig. 5b). The latter is identical to the dynamics in our sample without a Pt capping layer. This proves that the different timescales are indeed exclusively related to the excitation conditions of FeRh and not to different transition temperatures or other differences originating from the sample growth.

Interpreting the direct and indirect excitation

Irrespective of the excitation condition, we find that the FM phase rises on a single exponential timescale. According to the Avrami model of phase transitions[55] this is the expected behavior if FM domains nucleate at independent sites with a fixed probability. The probability as well as the corresponding timescale of this stochastic process can be described by an Arrhenius activation over an energy barrier[55,56], whose height is proportional to the nucleation timescale.

The timescales of 8 and 50 ps associated with the non- and near-equilibrium pathways of the phase transition in FeRh are consistent with our previous observation of a two-step rise of the FM phase in an inhomogeneously photo-excited thick FeRh film[38] that can be conceptually separated into two regions (i) the directly photo-excited near surface region and (ii) the lower lying regions only excited via heat transport. The corresponding depth-dependent activation of the non- and near-equilibrium pathways explains why previous UXRD experiments on thick FeRh films reported different rise times for different probing depth[35,37].

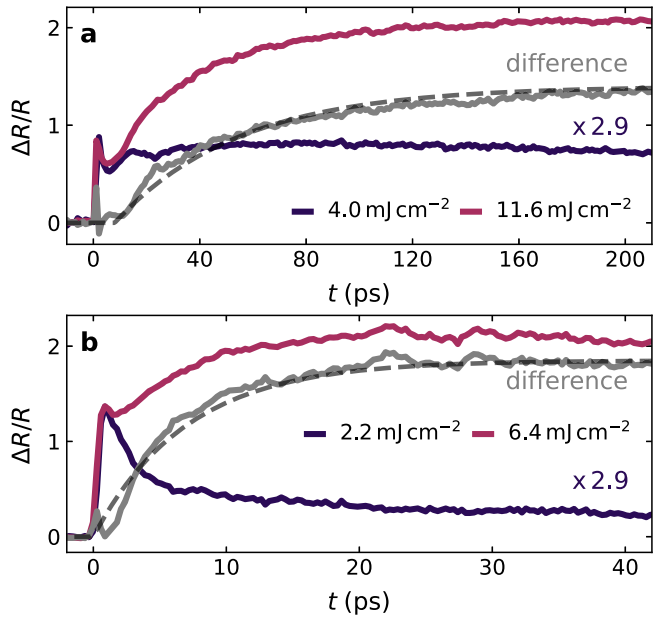

Fig. 5 | Transient reflectivity verifies the role of the excitation condition. The transient reflectivity of the FeRh film with a Pt capping layer probed through the MgO substrate upon a below- (purple) and above-threshold (pink) excitation from **a** the Pt side and **b** the substrate side. The below-threshold response (purple) is scaled to the above-threshold fluence to extract the contribution of the laser-induced phase transition by the difference (gray) as for the ultrafast x-ray diffraction (UXRD) experiment or in previous transient reflectivity experiments[30]. Upon excitation from the Pt side (as in the UXRD experiment), we observe a delayed rise of the FM phase on the 50 ps timescale (dashed line). In contrast, if FeRh is directly photo-excited through the substrate, the ferromagnetic (FM) phase rises on the 8 ps timescale (dashed line) in perfect agreement with the response of the sample without Pt capping layer.

The observation of the 8 ps timescale upon direct photo-excitation of FeRh, regardless of the maximum electron temperature (related to the pump-pulse duration), contrasts with the 50 ps timescale observed when the electrons in FeRh are heated to high temperatures via rapid near-equilibrium heat transport. This difference highlights the critical role of photo-induced electrons and holes beyond a Fermi distribution in driving the ultrafast phase transition in FeRh.

This supports the previous theoretical prediction that the laser-induced change of Fe-Rh hybridization and the resulting charge and spin transfer among Fe- and Rh-sites play a crucial role for the rapid modification of the electronic band structure[33]. The important role of Fe-Rh hybridization in FeRh was recently demonstrated by destabilizing the AFM state via spin polarized conduction band electrons that induced a short-lived Rh magnetic moment[57]. Other experiments also demonstrated a transfer of spin angular momentum via conduction band electrons from an adjacent Cu layer upon a photo-induced phase transition in FeRh[58].

Based on the literature our results suggest the following series of events: First, the photo-induced non-thermal electron distribution with charge carriers excited far from the Fermi energy modifies the Fe-Rh hybridization leading to a rapid modification of the electronic band structure[33]. This non-equilibrium state of FeRh lowers the energy barrier between the AFM and FM phase which reduces the nucleation timescale compared to near-equilibrium heating. Subsequently, FM domains exhibiting the larger lattice constant and a net magnetization nucleate on the identified 8 ps timescale at independent sites within the photo-excited region of the FeRh layer[56,59]. The magnetization of the nucleated FM domains initially points along random directions, which precludes the buildup of a macroscopic magnetization. This is followed by domain expansion and coalescence, where finally FM domains align within an external magnetic field via domain wall motion forming a macroscopic magnetization within hundreds of picoseconds[34–36].

The 8 ps nucleation timescale quantitatively matches the appearance of FM domains in resonant small-angle x-ray scattering experiments[59] and is on the same order of magnitude as the rise of the magnetization in magneto-optical Kerr effect experiments with strong magnetic fields up to 25 T that suppress the slow alignment of the nucleated domains[56]. Such strong magnetic fields influence the energy barrier between AFM and FM state, which may explain the slightly faster nucleation observed in these experiments.

Conclusion

In summary, we studied the laser-induced magnetostructural AFM-FM phase transition in FeRh upon direct photo-excitation with variable pump pulse duration and upon indirect excitation via heat transport from an adjacent opaque Pt capping layer. Irrespective of the pump pulse duration up to 10.5 ps, which exceeds the electron–phonon coupling time by far, we find the FM phase to nucleate on an 8 ps timescale when the photons are directly absorbed in the FeRh film. In contrast, the excitation of FeRh with thermalized electrons optically generated in a Pt cap layer leads to the rise of the FM phase on a 50 ps timescale. This experimentally identifies the important role of photo-induced non-thermal electron distributions for the pathway of the laser-induced phase transition in FeRh.

Our experiments with picosecond pump pulses illustrate that this approach is generally useful to identify the non-linear threshold behavior of (first-order) phase transitions and to disentangle the role of non-thermal and strongly heated but thermalized electrons for (phase transition) dynamics.

Methods

Sample growth and characterization

Nominally 12 nm-thick epitaxial FeRh(001) films were grown by magnetron sputtering from an equiatomic FeRh target[40] on double-side polished MgO(001) substrates. The second sample is capped by a 31.6 nm thick Pt(001) layer. The FeRh layer thicknesses were measured via x-ray reflectometry to be 12.3 and 12.6 nm for the uncapped and Pt-capped samples, respectively. We used synchrotron radiation from the KMC-3 XPP endstation at BESSY II[60] to characterize the first-order AFM-FM phase transition of the FeRh films by measuring the change in the average out-of-plane lattice constant d (symbols in Fig. 1b, d). The hysteresis for this locally probed lattice constant is narrower than the global temperature-dependent magnetization M_{FeRh} (solid line) determined by vibrating sample magnetometry using a QuantumDesign VersaLab magnetometer. To avoid intermixing of Pt and FeRh, the Pt capping layer was deposited at room temperature once the FeRh film was cooled down after annealing. Despite the lower growth temperature used for Pt, it partially grows epitaxially on top of the FeRh layer. Pt has a lattice parameter of 3.92 Å, which is smaller than that of MgO substrate (4.21 Å). Considering the 45° rotated epitaxial growth of Pt(001) on FeRh(001), the mismatch is −7 %. The resulting growth-induced in-plane compression is expected to lead to the observed increase of the transition temperature[25,40] in Fig. 1. Both FeRh films studied here show a sizable room-temperature residual FM phase, which amounts to 20 % of the maximum magnetic moment in the fully FM phase. Earlier works have identified the existence of FM stabilized regions both at the surface[43] and the film-substrate interface[44], with the latter reaching thicknesses up to 6 to 8 nm. This interfacial residual FM region likely originates from Fe diffusion into the MgO substrate and its suppression does not seem so far feasible[44,45]. An estimated 2.5 nm equivalent thickness of the residual FM region in the 12 nm-thick films highlights the good quality of our samples.

UXRD experiment

The UXRD experiments on both FeRh samples were performed at room temperature (295 K) without an external magnetic field in a co-planar symmetric diffraction geometry. The independence of the results for magnetic fields up to 1 T was previously confirmed[38]. The p-polarized pump pulses with a central wavelength of 800 nm are incident at 40° with respect to

Table 1 | Literature values for the physical parameters of the strain model

	Pt	FeRh	MgO
δ_p (nm)	9[42]	15[39]	inf
γ^S (mJ cm^{-3} K^{-2})	0.73[61]	0.16[62]	-
C_{ph} (J cm^{-3} K^{-1})	2.85[63]	3.48[50]	3.32[64]
κ_{el}^0 (W m^{-1} K^{-1})	66[65]	45	-
κ_{ph} (W m^{-1} K^{-1})	5.0[65]	5.0	50[66]
g (PW m^{-3} K^{-1})	375[67]	900[68]	-
ρ (g cm^{-3})	21.45	9.93	3.58
v_S (nm ps^{-1})	4.0[69]	5.0	9.1[70]
Γ_{el}	1.2[71]	1.4	-
Γ_{ph}	2.6[72]	1.7[73]	1.7[74]

The optical penetration depth δ_p, the Sommerfeld constant γ^S, the heat capacity per volume of the phonons C_{ph}, the electron–phonon coupling constant g, and the electron κ_e^0 and phonon κ_{ph} heat conductivity determine the spatio-temporal energy distribution upon laser-excitation in the framework of a diffusive 2TM[48]. The subsystem-specific Grüneisen parameters Γ_{el} and Γ_{ph} linearly relate the spatio-temporal energy density to an elastic stress on the lattice driving a quasi-static expansion and strain pulses propagating with sound velocity v_S according to the elastic wave equation[48]. We additionally reduced the phonon conductivity of the first MgO unit cell to 0.5 W m^{-1} K^{-1} and the electron conductivity of the last Pt unit cell to 0.5 W m^{-1} K^{-1} to mimic an interface resistance[48].

the sample normal with a repetition rate of 1 kHz and a beam footprint of 1300×1000 μm^2. We vary the pump-pulse duration between 60 fs and 10.5 ps for the FeRh sample without Pt capping layer by detuning a grating compressor. The sample with Pt capping layer is excited by 60 fs pump pulses. The temporal overlap of pump and probe and the duration of the picosecond pump pulses are independently determined by the laser-induced response of a metal-insulator superlattice that serves as a reference sample[47]. To probe the strain response of the Pt layer we kept fixed the incident angle θ of the 200 fs-long hard x-ray probe pulses with a photon energy of ≈8 keV provided by a table-top laser-based plasma x-ray source at 23.2°. The footprint of the x-ray probe pulse (600×300 μm^2) is approximately seven times smaller than that of the pump pulse which ensures a laterally homogeneous excitation of the probed volume. To probe the strain response of the FeRh layers, we performed symmetric θ–2θ scans around the (002) Bragg reflection at 31° for each pump-probe delay. The diffracted intensity is recorded by a DECTRIS PILATUS 100 k area detector. The lattice constant measured without laser excitation deviates less than 10^{-4} from the values measured for the highest fluence at $t < 0$, i.e., with the laser exciting the sample 1 ms before fs-probing. This means that the quasi-static heating of the laser is well below 5 K so FeRh recovers after each laser pulse to its initial AFM state. In agreement with previous UXRD experiments[37], the threshold fluence of the laser-induced phase transition is defined by the onset of the non-linear dependence of the lattice expansion on the excitation fluence. The precise determination of the threshold fluence is, however, unnecessary. It is sufficient to compare the above-threshold measurements to data obtained clearly below the threshold as estimated from the induced temperature jump.

Modeling strain response

We model the laser-induced transient strain response by utilizing the modular PYTHON library UDKM1DSIM[49] and literature values for the thermoelastic parameters in Table 1. In the first step, we calculate the optical absorption using a transfer matrix model and consider the excitation geometry in the experiment and the refractive indices $n_{MgO} = 1.72$, $n_{Pt} = 0.5762 + 9.5776i$ and $n_{FeRh} = 4.12 + 5.25i$. The latter was determined from ellipsometry on a comparable FeRh film. We describe the subsequent transfer of the deposited energy among electrons and phonons as well as different regions of the sample in the framework of a diffusive 2TM[48]. The calculated spatio-temporal energy density in the electrons and phonons are linearly related to stress contributions via subsystem-specific Grüneisen parameters. Their superposition drives the lattice response according to the elastic wave equation. Finally, we calculate the corresponding shift of the layer-specific Bragg peaks via dynamical x-ray diffraction. This shift is then compared to the measured strain response in Figs. 2 and 4.

All-optical experiment

In the all-optical pump-probe experiment, the Pt-FeRh-MgO sample is excited by a 100 fs-long p-polarized pump pulse with a central wavelength of 800 nm and a footprint of 800×800 μm^2 under normal incidence either from the Pt or the MgO-side. We probe the laser-induced change of the reflectivity with a 100 fs-long p-polarized probe pulse with a central wavelength of 400 nm and a footprint of 80×80 μm^2 under normal incidence. We compare the probe pulse reflected from the sample with an unperturbed reference pulse in a balanced photo-diode to enhance the signal-to-noise. Furthermore, we mechanically chop the pump pulses to 0.5 kHz and compare the pumped and unpumped reflectivity of the FeRh film.

Data availability

All data shown in the publication and additional data from the measurement series together with the evaluation and modeling scripts are archived under the https://doi.org/10.5281/zenodo.14937744.

Received: 18 October 2024; Accepted: 24 March 2025;
Published online: 08 April 2025

References

1. Weber, S. T. & Rethfeld, B. Phonon-induced long-lasting nonequilibrium in the electron system of a laser-excited solid. *Phys. Rev. B* **99**, 174314 (2019).
2. Maldonado, P. et al. Tracking the ultrafast nonequilibrium energy flow between electronic and lattice degrees of freedom in crystalline nickel. *Phys. Rev. B* **101**, 100302 (2020).
3. Mueller, B. Y. & Rethfeld, B. Thermodynamic μ*t* model of ultrafast magnetization dynamics. *Phys. Rev. B* **90**, 144420 (2014).
4. Eich, S. et al. Band structure evolution during the ultrafast ferromagnetic-paramagnetic phase transition in cobalt. *Sci. Adv.* **3**, e1602094 (2017).
5. Weißenhofer, M. & Oppeneer, P. M. Ultrafast demagnetization through femtosecond generation of non-thermal magnons. *Adv. Phys. Res.***11**, 2300103 https://doi.org/10.1002/apxr.202300103 (2024)
6. Shokeen, V. et al. Real-time observation of non-equilibrium phonon-electron energy and angular momentum flow in laser-heated nickel. *Sci. Adv.* **10**, eadj2407 (2024).
7. Sokolowski-Tinten, K. et al. Femtosecond x-ray measurement of coherent lattice vibrations near the lindemann stability limit. *Nature* **422**, 287–289 (2003).
8. Jung, C. et al. Inducing thermodynamically blocked atomic ordering via strongly driven nonequilibrium kinetics. *Sci. Adv.* **7**, eabj8552 (2021).
9. Wall, S. et al. Tracking the evolution of electronic and structural properties of VO_2 during the ultrafast photoinduced insulator-metal transition. *Phys. Rev. B* **87**, 115126 (2013).
10. Johnson, A. S. et al. Ultrafast x-ray imaging of the light-induced phase transition in VO_2. *Nat. Phys.* **19**, 215–220 (2023).
11. Kogar, A. et al. Light-induced charge density wave in $LaTe_3$. *Nat. Phys.* **16**, 159–163 (2020).
12. Thielemann-Kühn, N. et al. Optical control of 4f orbital state in rare-earth metals. *Sci. Adv.* **10**, eadk9522 (2024).
13. Wall, S. et al. Ultrafast changes in lattice symmetry probed by coherent phonons. *Nat. Commun.* **3**, 721 (2012).
14. de la Torre, A. et al. Colloquium: Nonthermal pathways to ultrafast control in quantum materials. *Rev. Mod. Phys.* **93**, 041002 (2021).
15. Johnson, A. S. et al. All-optical seeding of a light-induced phase transition with correlated disorder. *Nat. Phys.* **20**, 970–975 (2024).

16. Davies, C. et al. Phononic switching of magnetization by the ultrafast barnett effect. *Nature* **628**, 540–544 (2024).
17. Dewhurst, J. K., Elliott, P., Shallcross, S., Gross, E. K. & Sharma, S. Laser-induced intersite spin transfer. *Nano Lett.* **18**, 1842–1848 (2018).
18. Willems, F. et al. Optical inter-site spin transfer probed by energy and spin-resolved transient absorption spectroscopy. *Nat. Commun.* **11**, 871 (2020).
19. von Korff Schmising, C., Jana, S., Zülich, O., Sommer, D. & Eisebitt, S. Direct versus indirect excitation of ultrafast magnetization dynamics in FeNi alloys. *Phys. Rev. Res.* **6**, 013270 (2024).
20. De Jong, S. et al. Speed limit of the insulator–metal transition in magnetite. *Nat. Mater.* **12**, 882–886 (2013).
21. Polesya, S., Mankovsky, S., Ködderitzsch, D., Minár, J. & Ebert, H. Finite-temperature magnetism of FeRh compounds. *Phys. Rev. B* **93**, 024423 (2016).
22. Wegkamp, D. et al. Instantaneous band gap collapse in photoexcited monoclinic VO_2 due to photocarrier doping. *Phys. Rev. Lett.* **113**, 216401 (2014).
23. Lewis, L., Marrows, C. & Langridge, S. Coupled magnetic, structural, and electronic phase transitions in FeRh. *J. Phys. D Appl. Phys.* **49**, 323002 (2016).
24. Feng, Z., Yan, H. & Liu, Z. Electric-field control of magnetic order: from FeRh to topological antiferromagnetic spintronics. *Adv. Electron. Mater.* **5**, 1800466 (2019).
25. Fina, I. & Fontcuberta, J. Strain and voltage control of magnetic and electric properties of FeRh films. *J. Phys. D: Appl. Phys.* **53**, 023002 (2019).
26. Zhu, X. et al. Recent developments on the magnetic and electrical transport properties of FeRh-and Rh-based heterostructures. *J. Phys. Condens. Matter* **34**, 144004 (2022).
27. Kittel, C. Model of exchange-inversion magnetization. *Phys. Rev.* **120**, 335 (1960).
28. Gu, R. & Antropov, V. Dominance of the spin-wave contribution to the magnetic phase transition in FeRh. *Phys. Rev. B* **72**, 012403 (2005).
29. Gruner, M., Hoffmann, E. & Entel, P. Instability of the rhodium magnetic moment as the origin of the metamagnetic phase transition in α- FeRh. *Phys. Rev. B* **67**, 064415 (2003).
30. Ju, G. et al. Ultrafast generation of ferromagnetic order via a laser-induced phase transformation in FeRh thin films. *Phys. Rev. Lett.* **93**, 197403 (2004).
31. Sandratskii, L. M. & Mavropoulos, P. Magnetic excitations and femtomagnetism of FeRh: A first-principles study. *Phys. Rev. B* **83**, 174408 (2011).
32. Barker, J. & Chantrell, R. W. Higher-order exchange interactions leading to metamagnetism in FeRh. *Phys. Rev. B* **92**, 094402 (2015).
33. Pressacco, F. et al. Subpicosecond metamagnetic phase transition in FeRh driven by non-equilibrium electron dynamics. *Nat. Commun.* **12**, 5088 (2021).
34. Bergman, B. et al. Identifying growth mechanisms for laser-induced magnetization in FeRh. *Phys. Rev. B* **73**, 060407(R) (2006).
35. Mariager, S. O. et al. Structural and magnetic dynamics of a laser induced phase transition in FeRh. *Phys. Rev. Lett.* **108**, 087201 (2012).
36. Li, G. et al. Ultrafast kinetics of the antiferromagnetic-ferromagnetic phase transition in FeRh. *Nat. Commun.* **13**, 2998 (2022).
37. Quirin, F. et al. Structural dynamics in FeRh during a laser-induced metamagnetic phase transition. *Phys. Rev. B* **85**, 020103(R) (2012).
38. Mattern, M. et al. Speed limits of the laser-induced phase transition in FeRh. *APL Mater.* **12**, 051124 (2024).
39. Mattern, M. et al. Accelerating the laser-induced phase transition in nanostructured FeRh via plasmonic absorption. *Adv. Funct. Mater.* **34**, 2313014 (2024).
40. Arregi, J. A., Caha, O. & Uhlíř, V. Evolution of strain across the magnetostructural phase transition in epitaxial FeRh films on different substrates. *Phys. Rev. B* **101**, 174413 (2020).
41. Zhukov, V. P., Chulkov, E. V. & Echenique, P. M. Lifetimes and inelastic mean free path of low-energy excited electrons in Fe, Ni, Pt, and Au: Ab initio GW+T calculations. *Phys. Rev. B* **73**, 125105 (2006).
42. Bergeard, N. et al. Tailoring femtosecond hot-electron pulses for ultrafast spin manipulation. *Appl. Phys. Lett.* **117**, 222408 (2020).
43. Pressacco, F. et al. Stable room-temperature ferromagnetic phase at the FeRh (100) surface. *Sci. Rep.* **6**, 22383 (2016).
44. Fan, R. et al. Ferromagnetism at the interfaces of antiferromagnetic FeRh epilayers. *Phys. Rev. B* **82**, 184418 (2010).
45. Chen, X. et al. Tunneling anisotropic magnetoresistance driven by magnetic phase transition. *Nat. Commun.* **8**, 449 (2017).
46. Schick, D. et al. Ultrafast reciprocal-space mapping with a convergent beam. *J. Appl. Crystallogr.* **46**, 1372–1377 (2013).
47. Schick, D. et al. Normalization schemes for ultrafast x-ray diffraction using a table-top laser-driven plasma source. *Rev. Sci. Instrum.* **83**, 025104 (2012).
48. Mattern, M. et al. Concepts and use cases for picosecond ultrasonics with x-rays. *Photoacoustics* **31**, 100503 (2023).
49. Schick, D. udkm1dsim–a python toolbox for simulating 1d ultrafast dynamics in condensed matter. *Comp. Phys. Commun.* **266**, 108031 (2021).
50. Richardson, M., Melville, D. & Ricodeau, J. Specific heat measurements on an fe rh alloy. *Phys. Lett. A* **46**, 153–154 (1973).
51. Ahn, Y. et al. X-ray nanodiffraction imaging reveals distinct nanoscopic dynamics of an ultrafast phase transition. *Proc. Natl. Acad. Sci.* **119**, e2118597119 (2022).
52. Fognini, A. et al. The influence of the excitation pulse length on ultrafast magnetization dynamics in nickel. *Struct. Dyn.* **2**, 024501 (2015).
53. Gatel, C. et al. Inhomogeneous spatial distribution of the magnetic transition in an iron-rhodium thin film. *Nat. Commun.* **8**, 15703 (2017).
54. Debenedetti, P. G. & Stillinger, F. H. Supercooled liquids and the glass transition. *Nature* **410**, 259–267 (2001).
55. Avrami, M. Kinetics of phase change. I general theory. *J. Chem. Phys.* **7**, 1103–1112 (1939).
56. Dolgikh, I. et al. Ultrafast emergence of ferromagnetism in antiferromagnetic ferh in high magnetic fields. *npj Spintron.* **3**, 5 (2025).
57. Hamara, D. et al. Ultra-high spin emission from antiferromagnetic FeRh. *Nat. Commun.* **15**, 4958 (2024).
58. Kang, K. et al. Spin current driven by ultrafast magnetization of FeRh. *Nat. Commun.* **14**, 3619 (2023).
59. Agarwal, N. *Ultrafast dynamics of electronic structure and domain nucleation during photo-induced phase transition in FeRh*, Ph.D. thesis, Universität Hamburg Hamburg (2022)
60. Rössle, M. et al. The time-resolved hard x-ray diffraction endstation KMC-3 XPP at BESSY II. *J. Synchrotron Radiat.* **28**, 948–960 (2021).
61. Hohlfeld, J. et al. Electron and lattice dynamics following optical excitation of metals. *Chem. Phys.* **251**, 237–258 (2000).
62. Tu, P., Heeger, A., Kouvel, J. & Comly, J. Mechanism for the first-order magnetic transition in the FeRh system. *J. Appl. Phys.* **40**, 1368–1369 (1969).
63. Shayduk, R. et al. Nanosecond laser pulse heating of a platinum surface studied by pump-probe x-ray diffraction. *Appl. Phys. Lett.* **109**, 043107 (2016).
64. Barron, T., Berg, W. & Morrison, J. On the heat capacity of crystalline magnesium oxide. *Proc. R. Soc. Lond. Ser. A Math. Phys. Sci.* **250**, 70–83 (1959).
65. Duggin, M. The thermal conductivities of aluminium and platinum. *J. Phys. D Appl. Phys.* **3**, L21 (1970).
66. Slifka, A. J., Filla, B. J. & Phelps, J. Thermal conductivity of magnesium oxide from absolute, steady-state measurements. *J. Res. Natl. Inst. Stand. Technol.* **103**, 357 (1998).
67. Zahn, D., Seiler, H., Windsor, Y. W. & Ernstorfer, R. Ultrafast lattice dynamics and electron–phonon coupling in platinum extracted with a

global fitting approach for time-resolved polycrystalline diffraction data. *Struct. Dyn.* **8**, 064301 (2021).
68. Günther, S. et al. Testing spin-flip scattering as a possible mechanism of ultrafast demagnetization in ordered magnetic alloys. *Phys. Rev. B* **90**, 180407(R) (2014).
69. MacFarlane, R., Rayne, J. & Jones, C. Temperature dependence of elastic moduli of iridium. *Phys. Lett.* **20**, 234–235 (1966).
70. Durand, M. A. The temperature variation of the elastic moduli of NaCl, KCl, and MgO. *Phys. Rev.* **50**, 449 (1936).
71. Jarecki, J. et al. Controlling effective field contributions to laser-induced magnetization precession by heterostructure design. *Commun. Phys.* **7**, 112 (2024).
72. Nix, F. & MacNair, D. The thermal expansion of pure metals. ii: molybdenum, palladium, silver, tantalum, tungsten, platinum, and lead. *Phys. Rev.* **61**, 74 (1942).
73. Ibarra, M. & Algarabel, P. Giant volume magnetostriction in the FeRh alloy. *Phys. Rev. B* **50**, 4196 (1994).
74. White, G. & Anderson, O. Grüneisen parameter of magnesium oxide. *J. Appl. Phys.* **37**, 430–432 (1966).

Acknowledgements

We acknowledge the DFG for financial support via Project-no. 328545488 - TRR 227, project A10, the BMBF for funding via 05K22IP1 and the Leibniz Association for funding through the Leibniz Junior Research Group J134/2022. J. A. A. and V. U. acknowledge Project no. CZ.02.01.01/00/22_008/0004594 (TERAFIT). Access to the CEITEC Nano Research Infrastructure was supported by the Ministry of Education, Youth and Sports (MEYS) of the Czech Republic under the project CzechNanoLab (LM2023051). Beamtimes at the KMC-3 XPP endstation of the synchrotron radiation facility BESSY II at the Helmholtz Zentrum Berlin were required for thorough sample characterization.

Author contributions

M. M. and S.-P. Z. carried out the UXRD experiments. M. M. originally conceived the experimental idea and performed the data analysis and the modeling of the strain response yielding the transient FM volume fraction. M. R. measured the temperature-dependent lattice constant of FeRh and M. M. recorded and analyzed the all-optical reflectivity data. J. A. A. and V. U. grew the samples and carried out structural and magnetic characterizations. M. M. and M. B. prepared the manuscript. All authors worked on the manuscript.

Funding

Open Access funding enabled and organized by Projekt DEAL.

Competing interests

The authors declare no competing interests.

Additional information

Correspondence and requests for materials should be addressed to Matias Bargheer.

Peer review information *Communications Physics* thanks Rajasekhar Medapalli and the other, anonymous, reviewer(s) for their contribution to the peer review of this work.